Broadband measurements of the surface impedance in ferromagnetic wires as a boundary condition for scattering problems

Azim Uddin[1], Faxiang Qin[1,*], Diana Estevez[1,2], Konstantin Gorbatov[3], Yujie Zhao[4], and Dmitriy Makhnovskiy[5]

[1]*Institute for Composites Science Innovation (InCSI), School of Materials Science & Engineering, Zhejiang University, 38 Zheda Road, Hangzhou, 310027, China.*
[2]*Ningbo Innovation Centre, Zhejiang University, 1 South Qianhu Road, Ningbo, 315100, China.*
[3]*Lisi Aerospace, 38 Butlers Leap, Rugby, Warks CV21 3RQ, England.*
[4]*School of Physics and Astronomy, University of St. Andrews, Fife KY16 9SS, Scotland.*
[5]*Sensing Materials Technology Ltd, 44 St. Michael's Close, Plymouth, Devon PL1 4RX, England.*

[*] Corresponding author: faxiangqin@zju.edu.cn

Abstract

In the cm-wave range, the skin depth is comparable to the micron radius of ferromagnetic wires and thus their magnetic and conductive properties will influence the scattered electromagnetic field. Solving the scattering problem by considering the complicated internal magnetic structure of the wire becomes unpractical. There is a need to develop hybrid methods when the external problem of scattering on an inclusion is solved together with the experimental impedance conditions on its surface. Herein, we propose an accurate broadband impedance measurement technique operating up to 15 GHz. The PCB measurement and calibration cells designed in this work allow flexibility in choosing external stimuli such as magnetic field, tensile stress, and heat. The experimental impedance can be then used as the boundary condition in electromagnetic simulations making it possible to model, predict and design wire-based composites using numerical solvers such as CST Studio Suite.

1. Introduction

Dynamic magnetic behaviour through magnetoimpedance (MI) effect [1] is an essential property to characterize the microwave response of different materials such as ferromagnetic microwires [2-6], ribbons [7], and thin films [8-10]. Apart from fundamental research interest, in the technological context materials exhibiting a large MI effect arise as field/stress-sensitive sensors that can be integrated into a wide range of devices [11-16]. Special emphasis has been placed on Co-based and Fe-based glass-coated microwires. The thin glass shell $(2-15$ microns) along with the magnetostriction (positive or negative) of the core alloy (diameter $5-30$ microns) determine their unique magnetic anisotropic and mechanical properties. The technology of continuous casting of such wires makes it possible to produce highly-flexible threads of kilometre length [17]. These features allow them to be used as functional fillers in composite materials to introduce electromagnetic functionalities in the microwave range (ultra-high frequency UHF and super high frequency SHF bands), such as field/stress tunability, cloaking, absorption and shielding [18-24]. Such plethora of functional materials and their increasing trend towards operating at broader bandwidth stimulate the development of accurate measurement techniques to characterize their MI and microwave behaviour. The most commonly used methods are based on shorted coaxial transmission lines [25-27], microstrip transmission lines (MTLs) and coplanar waveguides (CPWs) etched on printed circuit boards (PCB) [28-32] aided by vector network analysers (VNA). In the shorted coaxial lines, one end of the microwire is connected to the inner conductor, while the other end is connected to the ground of the coaxial cap. The alignment of the sample along the axis will determine the measurement accuracy. Except for testing under magnetic field, measurements with sample stretching or heating are hardly possible in such coaxial cells. MTLs consist of a metal-backed substrate of relative permittivity ε_r on top of which is a metal strip with its width determined by the characteristic impedance of the line [33]. The sample is usually mounted on the surface of a PCB in the gap between two aligned microstrips and connected to them by soldering or conducting painting/glue. This method works for elongated samples of various geometries (wire, film, or ribbon), which can be considered as a continuation of a microstrip waveguide, although with a different characteristic impedance. Mounting the sample on the surface of PCB allows the application of external stimuli, including magnetic field, heat, and tensile stress. Meanwhile, the CPW PCB cells have an additional ground plane on the side of the microstrips that improves signal integrity at higher frequencies. This plane is also convenient for adding shunt surface elements, such as SHORT and LOAD terminations, which can be used for calibration of the microstrip network. The CPW cells are suitable for another measurement

51 scheme where a thin and sufficiently wide sample (film or ribbon) is placed over the continuous

52 strip, covering only its central segment. Direct electrical contact with the strip is excluded by

53 introducing a subtle gap or isolating layer. The parameter of interest is no longer the impedance

54 of the sample itself, but its magnetic and dielectric properties, determined indirectly through

55 the measurement of S-parameters of the loaded waveguide segment [28].

56   VNA, coaxial cables, non-coaxial strips on PCB, and a non-lumped sample constitute

57 a cascaded network that requires a multi-stage calibration procedure. The ultimate goal is to

58 extend the reference plane directly to the sample. VNA and the cables can be calibrated using

59 the standard 12-term error correction model with the coaxial SHORT-OPEN-LOAD-THRU

60 (SOLT) terminations. The strip waveguides must be de-embedded based on different methods

61 [28,30,31,34]. In turn, an elongated sample over a continuous ground (or segment of a loaded

62 strip) constitutes a structure which waveguide properties must be considered when calculating

63 material parameters from the S-parameter measurements. The principles of multi-stage

64 calibration have already been implemented for thin film samples, where ferromagnetic

65 resonance (FMR) and permeability dispersion were of primary interest [28,31]. The study of

66 Bilzer *et al.* [28] is closely related to the method developed in our present work since the

67 waveguide properties of the loaded CPW segment were explicitly revealed there. The

68 measurements were carried out up to 14 GHz, which is of interest for microwave scattering

69 applications. However, this method requires an additional reference measurement when the

70 film sample is removed leaving a continuous strip, and thus cannot be applied to a wire sample.

71 In another method proposed by Gonzalez *et al*. [31], a thin film sample was electrically attached

72 to microstrips on the PCB surface. It was assumed that the per-unit-length resistance and

73 inductance (used as indicative parameters characterising FMR), could be derived from the

74 measured characteristic impedance and propagation exponent. However, it remained unclear

75 how the shunt capacitance and conductance (per unit length) were estimated, which are

76 required to solve the corresponding equations. The maximum measurement frequency was up

77 to only 3 GHz, which, given the sample length used (11 mm), does not allow to judge the

78 accuracy of the phase distortion compensation along the sample. A radical decrease in sample

79 length enables considering the sample as a lumped element without a phase incursion even at

80 higher GHz. Such measurements have been performed with short wires connected at the end

81 of an open coaxial connector between the core and the ground shell [35,36]. However, in very

82 short samples, the magnetic domain structure at the ends might significantly change both the

83 magnetostatic and high-frequency properties. Moreover, due to open-end parasitic capacitance

84 and radiation losses (which are not included in the calibration), the accuracy of impedance
85 measurements will deteriorate.

86   In this work, we develop a broadband method for measuring accurately the field and
87 stress dependencies of the surface impedance in ferromagnetic wires. The measurements in the
88 frequency range up to 15 GHz were performed on MTL cells. In contrast to Bilzer and
89 Gonzalez [28,31], the part of the network formed by the microstrip and the coaxial connector
90 on PCB was not assumed to be ideal. Its 3-term model was created using a calibration cell
91 where three reflection coefficients were measured from identical microstrips with surface
92 mount SOL terminations. Touchstone S1P files containing the reflection coefficients were then
93 created for such microstrips and uploaded to the VNA for automatic de-embedding. The phase
94 distortion along the sample was compensated numerically using a phase unwrapping technique.
95 The measured impedance dispersions were fitted with multi-pole dispersion models available
96 in CST Studio Suite and followed the Kramers-Kronig relations. Recently, it has been shown
97 that conventional impedance models [37,38] cannot accurately reproduce impedance response
98 in the transition from MHz to GHz [39]. Thus, these models have limited practical value in
99 modelling the microwave response in free space. However, with our reliable impedance
100 measurement technique, it would be possible to realise a hybrid approach [40], where the
101 experimental surface impedance is used to numerically solve the scattering problem of an
102 individual wire inclusion without considering its complex magnetic domain structure [41].
103 Such approach will enable designing wire-filled composites with desirable microwave
104 properties and predict their microwave response under external stress/temperature/field stimuli.

2. PCB measurement and calibration cells

106   We have explored two types of PCB measurement cells, straight and dogbone, shown
107 in Fig. 1. A cell consists of two microstrips on one side of the board, and a continuous copper
108 ground plane on the opposite side (Fig. 1a). The microstrips are soldered to SMA connectors
109 at the edge of the PCB. A straight wire sample is placed in the gap between the microstrips and
110 connected to them with conductive silver paint, which solidifies without additional heating.
111 Rogers's composite materials [42] are widely used for high-frequency PCB designs due to their
112 stable and isotropic dielectric properties with negligible temperature drift and low loss. Our
113 boards were made of RO4003-C composite with a thickness of 0.812 mm and dielectric
114 constant $D_k = 3.55$ over a broad frequency range and low dielectric losses. To calculate the
115 microstrip width, we used the online microwave calculator available on Rogers' website. For
116 the chosen D_k and thickness, the width of the microstrips was calculated as 1.742 mm,

117 providing a characteristic impedance close to 50 Ω over the whole frequency range. Further
118 rules for designing waveguide structures can be found in [33].

119   A simpler straight PCB cell allows the application of external stimuli such as magnetic
120 field and heating (Fig. 1b). Heating can be realized by local blowing of samples with hot air,
121 while cooling other parts of the cell, including SMA connectors. The dogbone cell (Fig. 1c)
122 has protrusions for gripping by the clamps of the stress machine that allows the transfer of
123 tensile stress to the sample through the elastic deformation of the PCB. After the sample was
124 connected to the microstrips, it can be additionally glued to the board for more efficient stress-
125 transfer. Simultaneously with stretching, the sample can be exposed to magnetic field and
126 heating. Each cell type has a fixed microstrip length, and the gap between microstrips can be
127 varied to accommodate samples of varying lengths (10 and 20 mm). The length of the sample
128 should be much longer than the end segments involved in the connection to the microstrips
129 (1-2 mm each from each side). Measurement of shorter wire samples would solve the problem
130 of phase incursion along them [35,36]. However, it may introduce significant distortions due
131 to the magnetic domains at the wire ends, as well as increasing uncertainty in the length outside
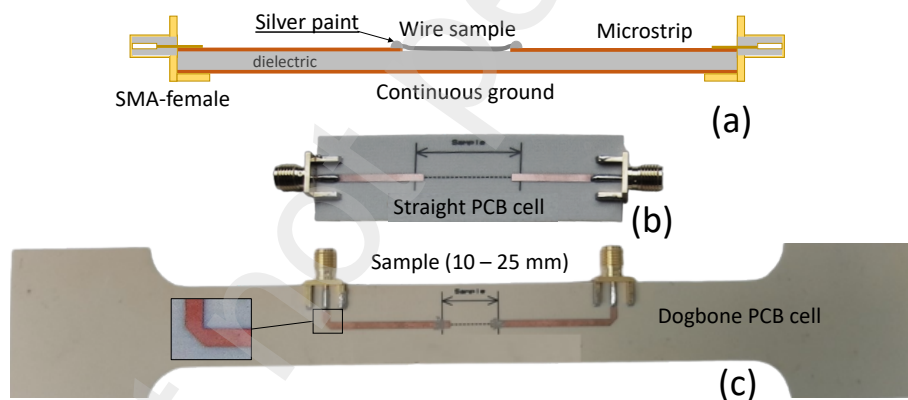132 the contact pads.

133

134 **Fig. 1.** PCB cells used for the impedance measurements (a) schematic diagram of the PCB
135   cell; (b) straight cell; (c) dogbone cell

136

137   Phase and amplitude distortions, including multiple reflections introduced by the
138 microstrips, will be compensated by de-embedding based on the 3-term error correction model.
139 This method requires three reflection coefficient (S_{11}) measurements from the microstrip with
140 SHORT, OPEN, and LOAD (50 Ω) surface mount terminations (SOL). Further details are
141 discussed in the following section. To provide such measurements, calibration cells were
142 developed for the straight (Fig. 2a) and dogbone (Fig. 2b) geometries. The microstrips on the

143 calibration cells were reproduced exactly as those on the measurement cells. OPEN termination
144 is just the open end of the microstrip. Up to several GHz, such termination will behave as an
145 ideal reflector with $S_{11O} = 1$ (linear magnitude). However, in the vicinity of 6 GHz, a
146 resonance was observed, indicating the need for a more accurate model. Apparently, already
147 starting from this frequency, it is necessary to consider the terminal parasitic capacitance, as
148 well as radiation losses from the open end which result in an effective impedance in series with
149 the capacitance. SHORT is a 0.3 mm via (copper plated hole) connecting the microstrip end
150 with the continuous ground on the opposite side of the board. This termination will behave like
151 a true reflector with $S_{11S} = -1$ (linear magnitude) well beyond 6 GHz. Further improvement
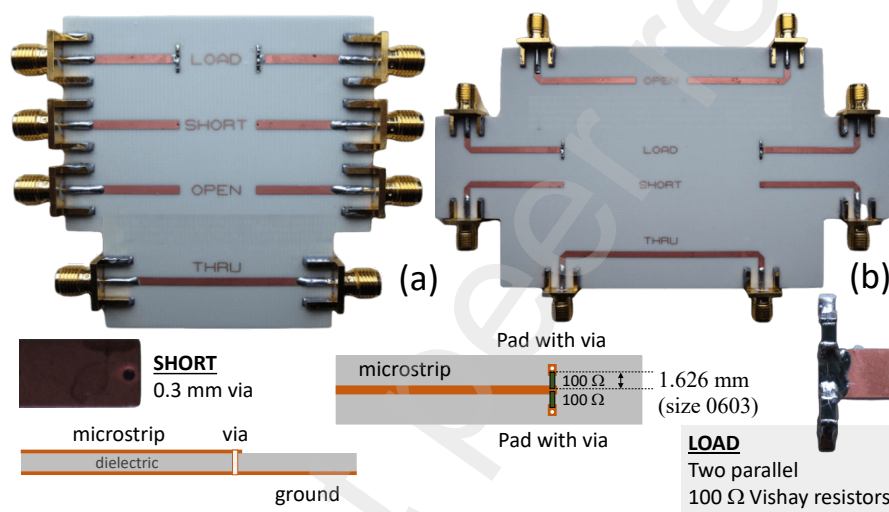152 of the model will require considering the parasitic inductance of the via and its skin effect.

153

154 **Fig. 2.** Two types of PCB calibration cells used for the 3-term error correction model. (a)
155 straight cell; (b) dogbone cell.

156

157 LOAD is two 100 Ω Vishay RF resistors (case size 0603) soldered in parallel between
158 the microstrip and two via-grounded pads, thus having 50 Ω. Such configuration is used to
159 reduce the parasitic inductance associated with them. Up to 15 GHz, S_{11L} of such resistor
160 termination may be as low as − 20 dB. Therefore, in the 3-term error correction model, we
161 assume that $S_{11L} = 0$ (linear magnitude). For RF resistors, Vishay provides LCR equivalent
162 circuits that could be used to model more accurately their S_{11L} as the terminations. However,
163 they still contain contact pads and vias for which the LCR parameters should also be considered.
164 Coplanar waveguide PCB cells could also be explored. Their calibration cells are more
165 convenient because SHORT and LOAD surface-mount terminations can be connected between
166 the microstrip and the adjacent ground planes on the same side. This plane is usually connected

167 to the main ground on the opposite side by a row of vias along the edge. Such arrangements
168 should minimise the parasitic parameters.

3. Multi-stage calibration for measuring the impedance of ferromagnetic wires on the PCB cells

171   The implemented calibration procedure, shown in Fig. 3, includes three stages: (i) full
172 2-port calibration of VNA and the cables attached to its ports using SOLT terminations (T
173 stands for THRU), (ii) de-embedding the microstrips using the 3-term error correction model,
174 and (iii) compensating the delay time along the sample using the unwrapped phase. The 2-port
175 SOLT calibration, also named TOSM in Rohde&Schwarz VNAs (M stands for MATCH), is
176 based on the 12-term error correction model which most fully describes the VNA error model
177 [43]. This type of calibration is implemented in all VNAs. All that is needed is a mechanical
178 calibration kit with SOLT coaxial standards and their analytical LCR models provided by the
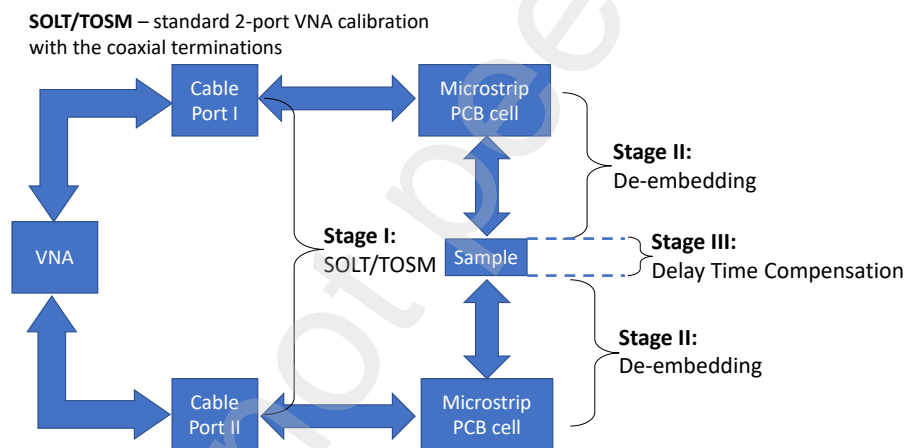179 VNA manufacturer.

180

181 **Fig. 3.** Multi-stage calibration for impedance measurements.

182

3.1. Stage I: SOLT calibration of VNA and cables

184   Once SOLT calibration is completed and activated, it will be automatically applied to
185 all measurements in real-time. At the Stage I, the reference plane has already been extended to
186 the end of the cables. Now all S-parameters of microstrips can be recovered using the 3-term
187 error model shown in Fig. 4. The model operates with only three error parameters: E_{DF}
188 (directivity forward), E_{RF} (reflection tracking forward), and E_{SF} (source mismatch forward).
189 The actual reflection S_{11A} produced by a termination connected to the microstrip end is
190 entangled into S_{11M} measured from the coaxial connection soldered to the PCB:

191 $$S_{11M} = \frac{b_1}{a_1} = E_{DF} + \frac{E_{RF}S_{11A}}{1 - S_{11A}E_{SF}}$$ (1),

192 where a_1 and b_1 represent input and output signals, respectively. By measuring three reflections

193 on the PCB calibration cell, where the microstrip is terminated with non-coaxial SOL, it

194 becomes possible to find E_{DF}, E_{RF}, and E_{SF}, and then recover all S-parameters of the microstrip.

195 Note that during these measurements the calibration cell is connected to the VNA and the
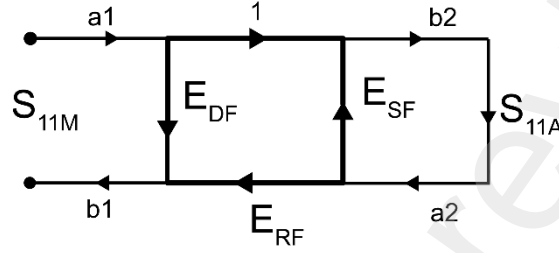
196 cables which have been already calibrated at Stage 1.

197

198 **Fig. 4.** 3-term error correction model. $a_{1,2}$ and $b_{1,2}$ represent input and output signals,

199 respectively.

200

201 In Eq. (1), we have three unknowns E_{DF}, E_{RF}, and E_{SF} which can be found from S_{11M}

202 measured from the three known termination standards SHORT ($S_{11A} \rightarrow S_{11S}$), OPEN ($S_{11A} \rightarrow$

203 S_{11O}), and LOAD ($S_{11A} \rightarrow S_{11L}$):

204 $$\begin{cases} S_{11MS} = E_{DF} + \frac{E_{RF}S_{11S}}{1 - S_{11S}E_{SF}} \\ S_{11MO} = E_{DF} + \frac{E_{RF}S_{11O}}{1 - S_{11O}E_{SF}} \\ S_{11ML} = E_{DF} + \frac{E_{RF}S_{11L}}{1 - S_{11L}E_{SF}} \end{cases}$$ (2).

205 After getting rid of the denominators, the system of Eq. (2) becomes linear with respect to three

206 variables: $x = E_{DF}$, $y = E_{SF}$, and $z = (E_{RF} - E_{DF}E_{SF})$:

207 $$\begin{cases} E_{DF} + S_{11MS}S_{11S}E_{SF} + S_{11S}(E_{RF} - E_{DF}E_{SF}) = S_{11MS} \\ E_{DF} + S_{11MO}S_{11O}E_{SF} + S_{11O}(E_{RF} - E_{DF}E_{SF}) = S_{11MO} \\ E_{DF} + S_{11ML}S_{11L}E_{SF} + S_{11L}(E_{RF} - E_{DF}E_{SF}) = S_{11ML} \end{cases}$$ (3).

208 For our terminations on the PCB calibration cells, we assumed $S_{11S} \equiv -1$, $S_{11O} \equiv 1$, and S_{11L}

209 $\equiv 0$ for the whole frequency range. If more accurate LCR models are available for the

210 terminations, the interpolated values can be used. Solving Eq. (3) numerically for each

211 frequency point within the sweep range set at SOLT of the VNA, all S-parameters of the

212 microstrip can be found for the whole frequency range: $S_{11} = x$, $S_{22} = y$, and $S_{21} = S_{12} = \pm$

213 $\sqrt{z + xy}$. The proper sign at the square root is chosen from the condition that the unwrapped

phase $\varphi = \pm \, arg\left(\sqrt{z + xy}\right)$ must have a negative slope. If the left and right microstrips are not symmetrical, the measurements and calculations described above must be performed for each microstrip.

3.2. Stage II: De-embedding microstrips

Modern VNAs allow embedding or de-embedding networks beyond the reference plane by an already established calibration. The microstrips can be considered as the networks connected beyond the reference plane at the cable ends. Thus, de-embedding them will extend the reference plane to the sample interface. A diagram explaining the principles of 2-port de-embedding is shown in Fig. 5. We follow the convention that S_{11} of a network faces the port to which it is connected.

$$\begin{pmatrix} b_2 \\ a_2 \end{pmatrix} = \widehat{\mathbf{P}}_1 \begin{pmatrix} a_1 \\ b_1 \end{pmatrix} \qquad \begin{pmatrix} b_4 \\ a_4 \end{pmatrix} = \widehat{\mathbf{P}}_A \begin{pmatrix} a_3 \\ b_3 \end{pmatrix} \qquad \begin{pmatrix} b_6 \\ a_6 \end{pmatrix} = \widehat{\mathbf{P}}_2 \begin{pmatrix} a_5 \\ b_5 \end{pmatrix}$$
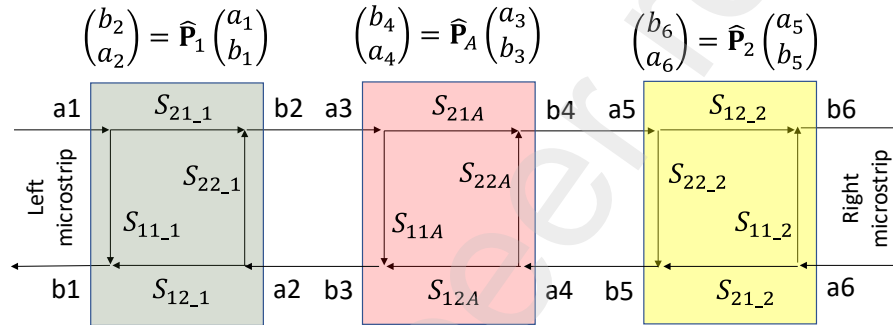

Fig. 5. Principles of 2-port de-embedding.

S-matrices do not allow performing calculations with cascaded networks, *i.e.* the product of the S-matrices of two cascaded networks is not equal to the S-matrix of the combined network. To carry out matrix calculations with cascading networks, we must operate with the propagation P-matrices, which can be introduced as follows:

$$\begin{pmatrix} b_2 \\ a_2 \end{pmatrix} = \widehat{\mathbf{P}} \begin{pmatrix} a_1 \\ b_1 \end{pmatrix} \tag{4}$$

It relates the input and output at the left with the input and output at the right. P-parameters can be expressed through S-parameters:

$$\widehat{\mathbf{P}} = \begin{pmatrix} \dfrac{S_{12}S_{21} - S_{22}S_{11}}{S_{12}} & \dfrac{S_{22}}{S_{12}} \\ -\dfrac{S_{11}}{S_{12}} & \dfrac{1}{S_{12}} \end{pmatrix} = \frac{1}{S_{12}} \begin{pmatrix} S_{12}S_{21} - S_{22}S_{11} & S_{22} \\ -S_{11} & 1 \end{pmatrix} \tag{5}$$

In turn, S-parameters can be expressed through P-parameters:

$$\widehat{\mathbf{S}} = \begin{pmatrix} -\dfrac{P_{21}}{P_{22}} & \dfrac{1}{P_{22}} \\ P_{11} - \dfrac{P_{12}P_{21}}{P_{22}} & \dfrac{P_{12}}{P_{22}} \end{pmatrix} \tag{6}$$

237 The sample stacked between two microstrips constitutes a combined network with the
238 propagation matrix $\hat{\mathbf{P}}_2\hat{\mathbf{P}}_A\hat{\mathbf{P}}_1$ (see Fig. 5):

$$239 \quad \begin{pmatrix} b_6 \\ a_6 \end{pmatrix} = \hat{\mathbf{P}}_2\hat{\mathbf{P}}_A\hat{\mathbf{P}}_1 \begin{pmatrix} a_1 \\ b_1 \end{pmatrix} = \hat{\mathbf{P}}_M \begin{pmatrix} a_1 \\ b_1 \end{pmatrix} \qquad (7).$$

240 Here, $\hat{\mathbf{P}}_1$ and $\hat{\mathbf{P}}_2$ are the known propagation matrices of the left and right microstrips
241 respectively, obtained using the PCB calibration cell, 3-term model, and Eq. (5). $\hat{\mathbf{P}}_A$ is the
242 unknown propagation matrix of the sample. On the other hand, $\hat{\mathbf{P}}_M = \hat{\mathbf{P}}_2\hat{\mathbf{P}}_A\hat{\mathbf{P}}_1$ of the combined
243 network can be obtained by measuring its S-parameters and using Eq. (5). Therefore, $\hat{\mathbf{P}}_A = \hat{\mathbf{P}}_2^{-1}$
244 $\hat{\mathbf{P}}_M\hat{\mathbf{P}}_1^{-1}$, where all three matrices at the right are known. Then, $\hat{\mathbf{P}}_A$ can be recalculated to $\hat{\mathbf{S}}_A$
245 using Eq. (6). Note that for the 2-port de-embedding, the whole matrix $\hat{\mathbf{S}}_M$ of the combined
246 network must be measured. Whereas, for the 1-port de-embedding, S_{11A} can be recovered from
247 S_{11M} (see Eq. (1)):

$$248 \quad S_{11A} = \frac{S_{11M} - E_{DF}}{E_{RF} + E_{SF}(S_{11M} - E_{DF})} \qquad (8).$$

249 In our measurement setup, we use Rohde&Schwarz (R&S) ZNB20 2-port VNA, 100
250 kHz – 20 GHz. In this VNA, the de-embedding can be performed automatically after uploading
251 the S2P Touchstone text file (.s2p) for each network. If the networks are symmetrical as in our
252 case, the same file can be uploaded for both ports. The S2P file includes the header # Hz S RI
253 R 50 and consists of nine tab-delimited columns: frequency [Hz], $\mathrm{Re}[S_{11}]$, $\mathrm{Im}[S_{11}]$, $\mathrm{Re}[S_{21}]$,
254 $\mathrm{Im}[S_{21}]$, $\mathrm{Re}[S_{12}]$, $\mathrm{Im}[S_{12}]$, $\mathrm{Re}[S_{22}]$, $\mathrm{Im}[S_{22}]$. We have developed a Python program code,
255 available at a public repository on GitHub [44], which creates S2P files of the microstrips from
256 $S_{11/22MSOL}$ (see Eq. (3)) measured from the PCB calibration cell. The surface-mount
257 terminations can be considered ideal or have dispersion behaviour saved in $S_{11/22SOL}$. Also, the
258 algorithm can perform the 1-port or 2-port de-embedding if this option is not available in an
259 old VNA model. Further details can be found in the manual on GitHub.

260 After activating SOLT calibration and de-embedding (Stages I and II), S_{11A} and S_{21A}
261 of the sample can be correctly measured. For the 1-port and 2-port measurements, the sample
262 impedance is calculated as follows:

$$263 \quad Z_A = 50 \times \frac{1 + S_{11A}}{1 - S_{11A}} [\Omega] \qquad (9),$$

$$264 \quad Z_A = 100 \times \frac{(1 - S_{21A})}{S_{21A}} [\Omega] \qquad (10).$$

265 However, these equations assume that the sample is lumped, *i.e.* it has zero electrical length,
266 or at least much shorter than the wavelength. This condition is not met in our case. A piece of
267 wire above a continuous ground is a waveguide structure resulting in a phase incursion.
268 Compensating for this phase incursion constitutes Stage III in our calibration procedure (Fig.
269 3), which will be explained next.

270 *3.3. Stage III: Phase unwrapping and delay time compensation along the wire sample*

271   Our measurement cells are 2-port. Typical phase dispersions of S_{21A} measured in
272 ferromagnetic wire samples on the straight and dogbone PCB cells are shown in Figs. 6(a, b),
273 respectively. Piecewise negative phase slopes separated by device induced jumps (phase can
274 be measured only within $[-\pi,\pi]$) are caused by the delay time along the wire. They may be
275 distorted due to parasitic resonances and deterioration in the de-embedding accuracy at higher
276 GHz frequencies. For any analysis and further processing, the phase must be free from 2π
277 jumps and returned to a continuous form with a negative slope. By fitting this slope in a certain
278 frequency range with a straight trend line $\varphi(f) = af + b$, where f is the frequency, the delay
279 time can be calculated as $\Delta t = |a|/(2\pi)$. Although phase unwrapping is available in modern
280 VNAs, performing it directly on the device may be difficult. When allocating a certain
281 frequency interval for unwrapping, VNA may show point spikes caused by numerical
282 uncertainties during de-embedding. These spikes will not allow the phase to be unwrapped
283 correctly. Therefore, it is desirable to save the raw phase dispersion over the entire range in a
284 csv/text file, truncate the frequency interval as proposed in Fig. 6, and then unwrap the phase
285 numerically. The corresponding Python algorithm is available at our public GitHub repository
286 in the folder Delay time [44]. To calculate the impedance using Eq. (10), S_{21A} must be replaced
287 by the corrected $\tilde{S}_{21A}(\omega) = S_{21A}(\omega) \times \exp(i\omega\Delta t)$. This completes the Stage III of calibration.
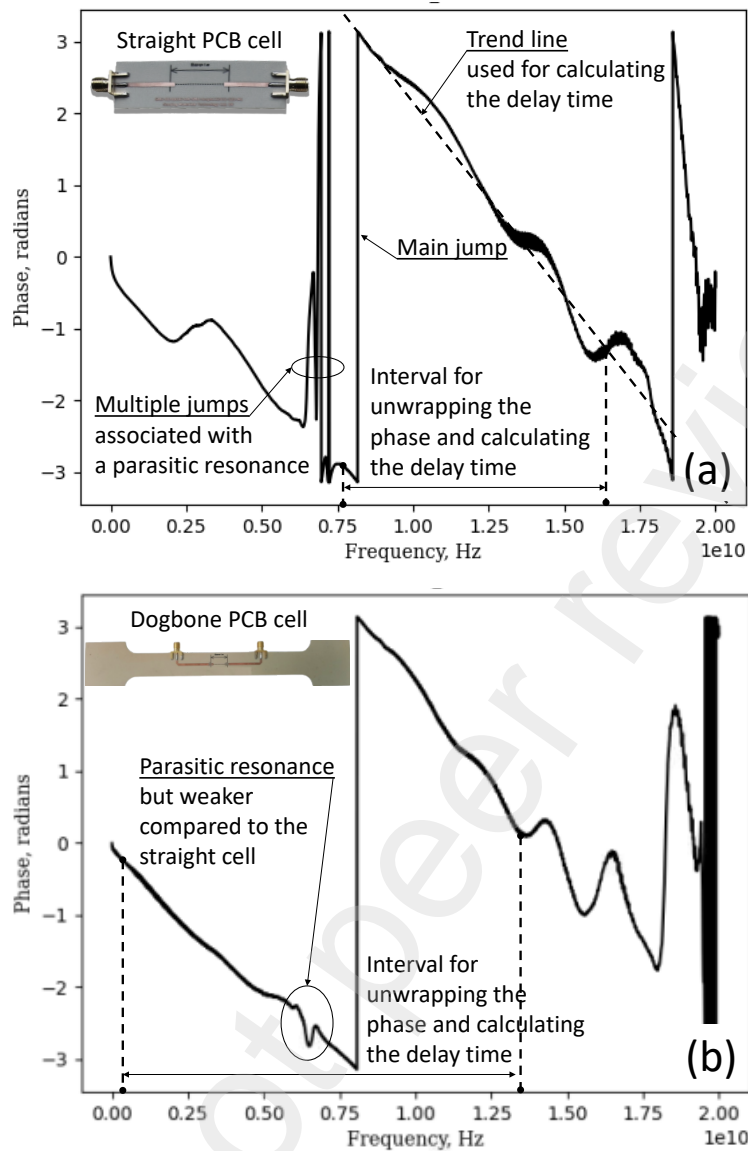
Fig. 6. Phase dispersions of S_{21A} measured in ferromagnetic wire samples on the straight (a) and dogbone (b) PCB cells.

3.4. Impedance measurement setup

To measure the impedance, we designed the setup shown in Fig. 7. It includes three programmable R&S devices: ZNB20 VNA (2-port, 100 kHz – 20 GHz), Function Generator HMF2550, and HMC 8012 Digital Multimeter (DMM). The only analog device is Accel Instruments Waveform Amplifier TS250-2 used for feeding a Helmholtz coil. All devices are mounted on a trolley, which allows the setup to be parked next to various installations, such as a stress machine or a bench with the coil. Impedance measurements require three programmable devices to operate in sync according to the block diagram shown in Fig. 8. The device control was implemented in LabVIEW 2015 through NI VISA driver. SOLT calibration

302 (Stage I) and de-embedding (Stage II) are already activated on VNA before starting
303 measurements. The program iterates the DC offset voltage at the output of the function
304 generator from its minimum $-V_g$ to maximum $+V_g$ with the specified number of points N.
305 The DC offset output is applied to the power amplifier to feed the Helmholtz coil. After
306 applying a voltage, the operation is paused for the time duration of $20 \times L/R$, where L and R
307 are the coil inductance and resistance, to achieve the saturation of the coil current. The VNA
308 sweep is then activated to measure $S_{21/11}$ at discrete frequency points (N_f). During this sweep,
309 the field is kept constant. The actual voltage applied to the coil after the power amplification is
310 measured by the DMM. Its value is passed to the program to be recalculated into the field using
311 the coil calibration coefficient (Oe/V). The real and imaginary parts of the measured S-
312 parameter are transferred as an array to the PC, where they are corrected to compensate for the
313 sample delay time (Stage III), and then converted into impedance using Eq. (9) or (10). The
314 measurement process is repeated in a loop for the next field point. To reproduce possible
315 magnetic hysteresis properties, the DC offset is iterated in both directions: from negative to
316 positive values (loop forward) and then in the inverse direction (loopback). Stress and
317 temperature measurements are currently not integrated into the control program. These
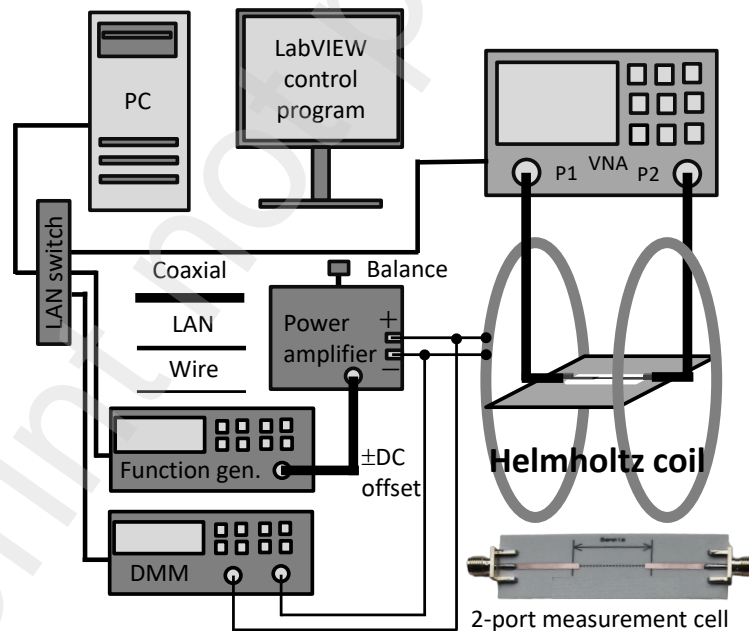318 parameters are changed manually after a loop over the field points is completed.

319

320 **Fig. 7.** Automated setup for measuring the field dependence of the impedance.
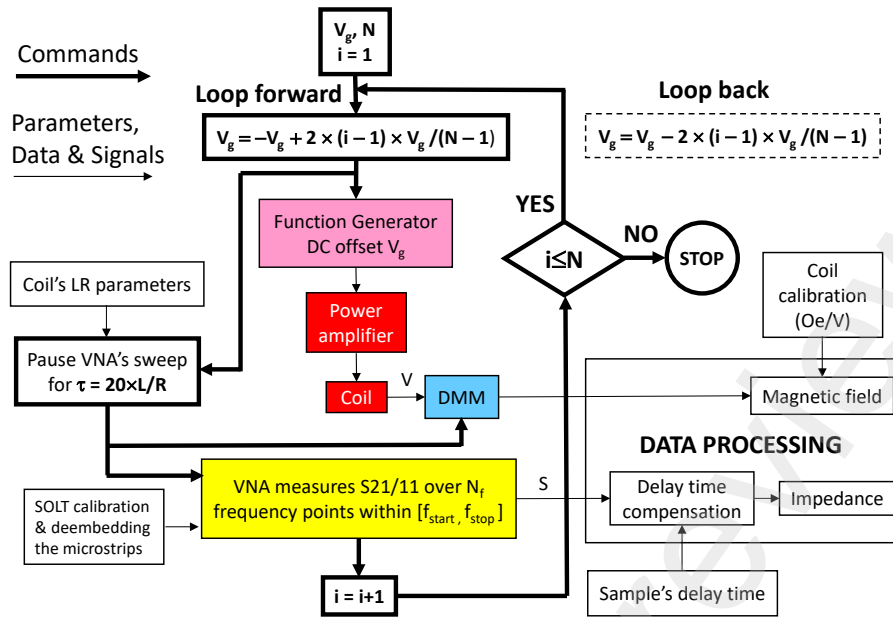
321

Fig. 8. Block diagram of the LabVIEW control program that synchronizes the operation of three R&S devices for measuring the field dependence of the impedance.

4. Broadband impedance measurement under in-situ magnetic field and stress

As an illustration of the proposed measurement technique, Fig. 9 shows a broadband dispersion of the impedance in a glass-coated ferromagnetic wire. The continuous wire reel, kindly provided by MFTI Ltd (Republic of Moldova), was fabricated by the Taylor-Ulitovskiy method [17] from a Co-based alloy of the composition $Fe_4Co_{68.7}Ni_1B_{13}Si_{11}Mo_{2.3}$ (wt.%) The total wire diameter, including the glass shell, was 23.2 μm with a metal core of 19.1 μm. A piece of wire 20 mm long was fixed on a dogbone PCB cell. The impedance was recalculated from $\tilde{S}_{21A}$ using Eq. (10) over the frequency range 1 MHz – 15 GHz in the presence of longitudinal DC bias fields. As will be shown in the next section, the uncertainty in determining the delay time along the sample used for the correction of S_{21A} (Stage III) does not exceed ± 3 ps or less than ± 0.5 mm in terms of the sample length.

In ferromagnetic wires, the magnetic AC permeability arises as a result of the magnetization precession induced by the circular magnetic field when passing a high-frequency current. Conductivity and effective AC permeability together determine the skin-depth for the high-frequency current. In Co-based glass-coated wires having negative magnetostriction, the equilibrium magnetisation has a circular direction which can be deflected by applying a moderate longitudinal DC magnetic field. This leads to a field dependence of the AC permeability and, as a result, the impedance [1]. The most noticeable effect in this type of wire is a broad FMR, which gradually develops when a longitudinal magnetic field is applied, as shown in Fig. 9. The impedance amplitude reaches its maximum value around 1 GHz when the

magnetisation is saturated along the wire axis. As FMR is not the subject of study in this work, we mention it only because in its vicinity the impedance will demonstrate maximum sensitivity to external stimuli, which is important for applications where tunable scattering properties are required.

In Fig. 10, the stress dependence of the impedance was measured in the vicinity of FMR at 900 MHz at different longitudinal bias fields. The dogbone PCB cell was stretched between the grippers of a desktop Instron machine. The strain was measured by an optical camera method [39]. On one hand, stress sensitivity requires the magnetisation to be deflected from the circular direction. Without external magnetic field, the stress sensitivity of impedance is negligible (yellow trace). On the other hand, magnetisation saturated along the wire axis by a strong longitudinal field will require a larger tensile stress to rotate it back into the circular direction. This tension may be outside the elastic regime. Thus, there should be an optimal longitudinal external field that provides the largest stress sensitivity of the impedance within the elastic regime. For the sample in Fig. 10, the optimal magnetic field which produces largest stress sensitivity of impedance is about 5.36 Oe.
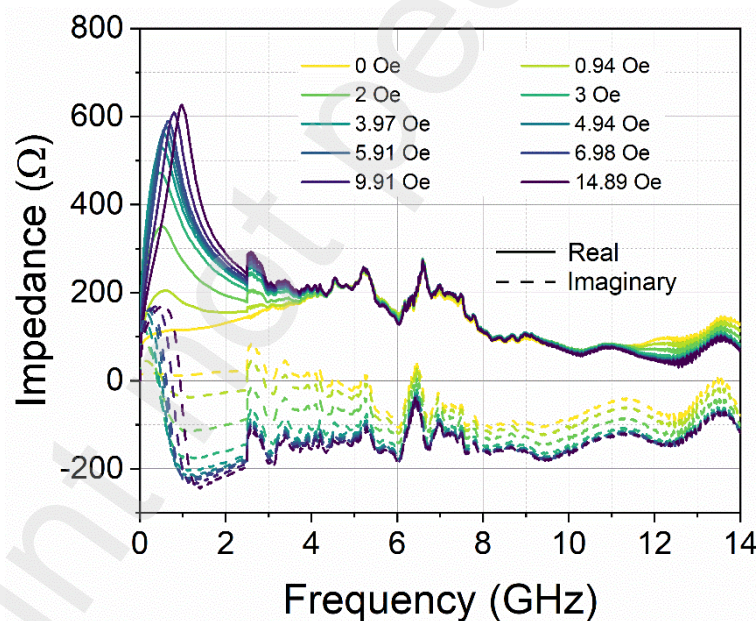

Fig. 9. Broadband dispersion of the impedance recalculated from the corrected $\tilde{S}_{21A}$ at different longitudinal bias fields. Three-stage calibration has been applied.
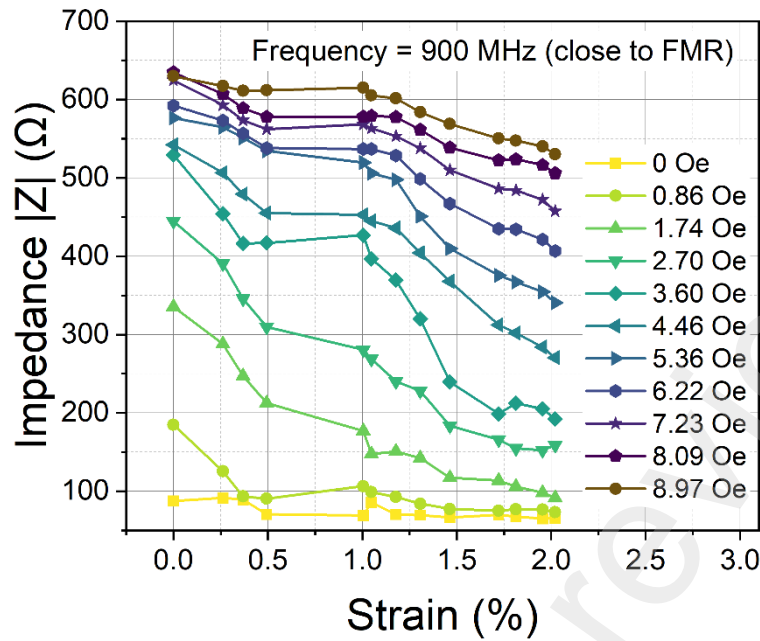
Fig. 10. Stress dependence of the wire impedance measured at a fixed frequency in the vicinity of FMR at different longitudinal bias fields.

5. Surface impedance of ferromagnetic wires as a boundary condition in scattering simulations

In the cm-wave range, the skin depth is comparable to the micron radius of the wire. The entire volume of the wire with its conductive and magnetic properties will be involved in the formation of the scattered electromagnetic field. Widely used models [37,38] cannot accurately reproduce MI properties in the frequency range of interest for scattering applications (transition from MHz to GHz). This prompts us to develop a method for measuring surface impedance as a boundary condition for scattering problems. The definition of the surface impedance tensor $\hat{\varsigma}$ given in CST coincides with that in Ref. [45]:

$$\overline{\mathbf{E}}_t = \hat{\varsigma}(\overline{\mathbf{H}}_t \times \mathbf{n}) \tag{11},$$

where the tangent vector of the total electric field $\overline{\mathbf{E}}_t$ at the wire surface is expressed through the vector product of the unit normal vector $\mathbf{n}$ directed inside the conductor and the tangent magnetic field $\overline{\mathbf{H}}_t$ at the wire surface. In the cylindrical coordinate system (x,φ,r) associated with the wire, the impedance boundary condition can be written in the coordinate form:

$$\begin{cases} \overline{E}_x = \varsigma_{xx}\overline{H}_\varphi - \varsigma_{x\varphi}\overline{H}_x \\ \overline{E}_\varphi = \varsigma_{\varphi x}\overline{H}_\varphi - \varsigma_{\varphi\varphi}\overline{H}_x \end{cases} \tag{12}.$$

384 In a nonmagnetic conductor, $\varsigma_{x\phi/\phi x} \equiv 0$. The presence of the off-diagonal components is a

385 distinctive feature of ferromagnetic samples with a certain type of magnetic anisotropy. The

386 use of these components for sensor applications in the MHz range has already been explored

387 previously [46]. A thin wire only allows one wave polarization that is essential for the

388 formation of a scattered field: with an electric vector along the wire. Therefore, $\varsigma_{x\varphi}\overline{H}_x$ in the

389 first equation in Eq. (12) can be neglected. The second equation in Eq. (12) defines the induced

390 circular current, which will introduce a negligibly smaller radiation additive compared to the

391 longitudinal induced current. Therefore, this equation can be neglected. Only one equation

392 remains essential for scattering problems: $\overline{E}_x = \varsigma_{xx}\overline{H}_\varphi$.

393 CST allows experimental impedance boundary conditions for solving external

394 electrodynamic problems. The impedance can be provided in a tabular form: frequency, real

395 part, and imaginary part. These values are then interpolated using a predefined template that

396 includes first and second-order resonant terms. When calculating the wire impedance Z from

397 the corrected $\tilde{S}_{21A}$, the delay time along the sample is fully compensated, thus reducing its

398 effective electrical length to zero. The total current I along such an ideal impedance element

399 does not have a longitudinal distribution, as well as $\overline{E}_x$. The circular magnetic field on the

400 surface of the wire is $\overline{H}_\varphi^{\text{SI}} = I/2\pi a = V/2\pi aZ = l\overline{E}_x/2\pi aZ$ (SI units) or $\overline{H}_\varphi^{\text{cgs}} = 2lI/ac = 2V/acZ$

401 $= 2l\overline{E}_x/acZ$ (cgs units). Here, a and l are the wire radius and length respectively, and $c =$

402 $2.99792458 \times 10^{10}$ cm/s is the speed of light (cgs). Using these equations, for the

403 longitudinal surface impedance $\varsigma_{xx} = \overline{E}_x/\overline{H}_\varphi$, we obtain:

404 $$\varsigma_{xx}^{\text{SI}}[\Omega/\text{sq}] = Z[\Omega] \times \frac{2\pi a}{l} \tag{13},$$

405 $$\varsigma_{xx}^{\text{cgs}}[(\text{s/cm})/\text{sq}] = Z[\Omega] \times \frac{10^9 a}{2lc} \tag{14}.$$

406 In Eq. (14), the normalization factor is chosen so that the impedance is measured in Ohms. The

407 notations Ω/sq and $(\text{s/cm})/\text{sq}$ adopted here refers to the surface (sq). The wire parameters a

408 and l can be measured in any units because they enter the equation as a ratio.

409 The CST Studio Suite (release version 2022.04) offers a multi-resonance physical

410 model along with numerical optimization to fit the experimental surface impedance dispersion:

411 $$\varsigma(\omega) = \varsigma_\infty + i\omega L + \sum_{n=1}^{N}\frac{\beta_{0,n}}{\alpha_{0,n} + i\omega} + \sum_{n=1}^{M}\frac{\gamma_{0,n} + i\omega\gamma_{1,n}}{\delta_{0,n} + i\omega\delta_{1,n} - \omega^2} \tag{15}$$

412 The fitting parameters have the following physical interpretations. The 1$^{\text{st}}$ order resonance

413 terms ($n = \overline{1,N}$): frequency of the pole $f_{p1,n} = \alpha_{0,n}/2\pi$ [Hz], static gain contribution $g_{1,n} =$

414 $\beta_{0,n}/\alpha_{0,n}$ [Ω/sq]. The 2$^{\text{nd}}$ order resonance terms ($n = \overline{1,M}$): resonance frequency $f_{p2,n} =$

$\sqrt{\delta_{0,n}}/2\pi$ [Hz], quality factor $Q_{2,n} = \sqrt{\delta_{0,n}}/\delta_{1,n}$, frequency of the zero $f_{z2,n} = \gamma_{0,n}/2\pi\gamma_{1,n}$ [Hz], static gain contribution $g_{2,n} = \gamma_{0,n}/\delta_{0,n}$ [Ω/sq]. The maximum number of resonant terms used for a fitting cannot exceed 10, including the order of the poles. For example, two resonances of 1st order and four resonances of 2nd order.

Fig. 11 illustrates the principles of impedance fitting used in CST. The dispersion curves for the real and imaginary parts of ς_{xx} in the presence of an external longitudinal bias field (3.97 Oe) were fitted with $\varsigma_\infty = 0.00647476$ Ω/sq, $L = 1.07214 \times 10^{-12}$ H, two resonance terms of 1st order, and three resonance terms of 2nd order. The physical parameters for the resonance terms are shown in Table 1. The total fitting order 8 was set in the program interface, and the choice of resonant terms between the 1st and 2nd orders was made automatically by the CST optimization algorithm. The fitting was able to identify and accurately describe the LC resonances $f_{p2,n}$ ($n = \overline{1,3}$), including the resonance at ~6.37 GHz ($f_{p2,2}$) caused by the measurement cell. The 1st order model is responsible for magnetic resonance properties, revealing two poles with $f_{p1,1} \approx 200$ MHz and $f_{p1,2} \approx 1$ GHz. The sum of these two terms decays as $1/\omega$ at $\omega \to \infty$ and proportional to ω at $\omega \to 0$ due to $g_{1,1}$ and $g_{1,2}$ having close absolute values and opposite signs. The gains $g_{2,n}$ ($n = \overline{1,3}$) are significantly smaller, and hence the 2nd order model contributes much less within the frequency range $[f_{p1,1}, f_{p1,2}]$.
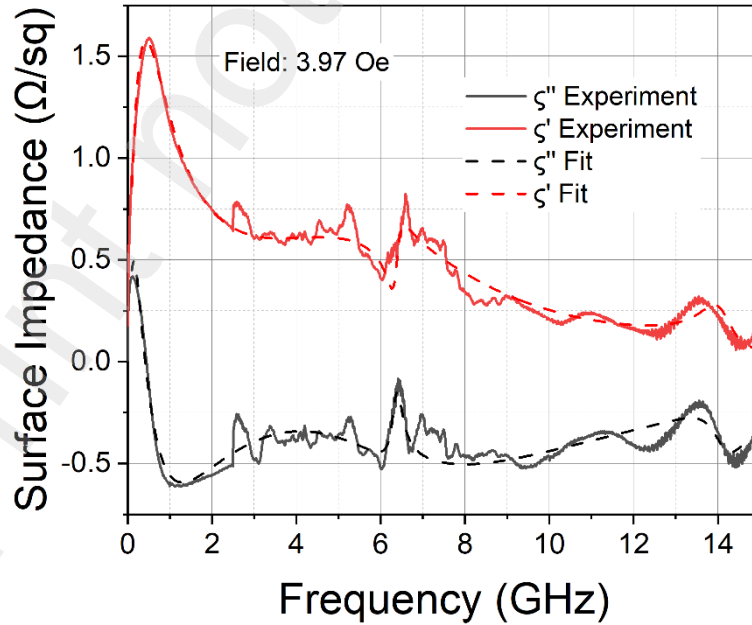

Fig. 11. The dispersion curves for the real and imaginary parts of ς_{xx} in the presence of an external longitudinal bias field 3.97 Oe fitted with the model template in Eq. (15).

Table 1. Physical parameters of the 1st and 2nd order resonance models used to fit the

impedance dispersion in Fig. 11.

N	1	2	3
f_{p1} [GHz]	0.200253	1.03141	
g_1 [Ω/sq]	-1.54142	1.76759	
f_{p2} [GHz]	14.1188	6.36786	6.76186
Q_2	14.6469	20.9207	0.965668
f_{z2} [GHz]	12.8863	15.2074	4.53192
g_2 [Ω/sq]	0.00964765	-0.014956	0.340934

When recalculating the corrected $\tilde{S}_{21A}$ into the impedance, even a slight error in the delay time (determined from the unwrapped phase), may violate physical conditions imposed on the impedance dispersion. Thus, further adjustment is needed to ensure that the real part of the impedance remains positive and tends to zero at higher GHz frequencies. As for the imaginary part of the impedance, it is not physically forbidden to go into the positive region. However, if a premature transition is exhibited caused by an error in the delay time, this will cause the real part to grow again, which will be noticeable. Ignoring these physical conditions makes impedance measurements practically useless [30]. An adjustment algorithm for the delay time is used here and available at GitHub repository in the folder Impedance dispersion [44]. As the frequency increases, both the real and imaginary curves are asymptotically approaching the horizontal axis, thereby reducing the tolerated uncertainty in the delay time. Our PCB cells allow de-embedding up to 15 GHz. We have found that for this frequency range, the delay time uncertainty cannot exceed $\pm$ 3 ps. This corresponds to $\pm$ 0.5 mm uncertainty in the sample length, given that the speed factor of wave propagation over PCB is ~0.6. In Fig. 12, the experimental solid curves of the real and imaginary parts of the impedance were reconstructed from $\tilde{S}_{21A}$ with the calculated and adjusted delay time. The shadows accompanying these central curves correspond to the impedance tolerance caused by the delay time uncertainty $\pm$ 3 ps, which does not violate the physical conditions, at least up to 15 GHz. The central curves (0 ps) and curves corresponding to the tolerance limits (+ 3 ps and − 3 ps) were fitted with the CST model template in Eq. (15). It can be seen that the fitting curves for 0 ps are better centred with respect to their parent experimental curves. Thus, fitting with the theoretical model can serve as an additional criterion for minimizing the error in the delay time. Compared with our measurements, the measurement proposed before was limited to 3 GHz [31], which do not allow any conclusions to be drawn about the accuracy of the phase

464 compensation along the sample. Also, there was no analysis carried out on the correspondence
465 of measurements to impedance models that would guarantee the fulfilment of the Kramers-
466 Kronig relations.
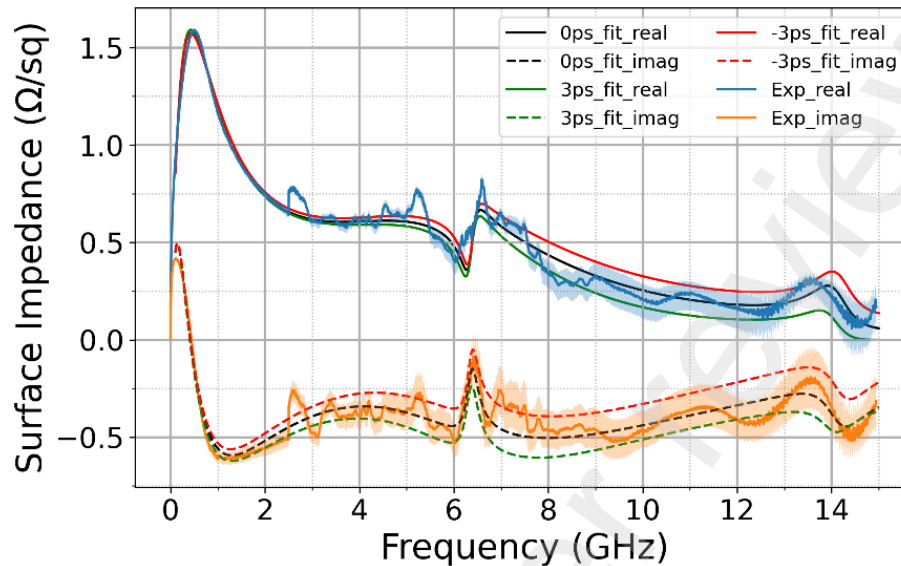

467
468 **Fig. 12.** The impedance tolerance caused by the uncertainty of the delay time.

469

470   It has been shown that for wires with a circular anisotropy, the impedance dependence
471 on the external longitudinal field at fixed frequencies cannot be described by existing models
472 in the MHz to GHz transition [39,47]. A typical impedance transformation scenario observed
473 in the experiment is shown in Fig. 13. Starting around 700 MHz, when the change in
474 impedance with field reaches its maximum, there is a bending point in the curve producing a
475 double slope (800 MHz). As the frequency increases, the bending point remains fixed relative
476 to the field axis, while the maximum shifts toward higher fields. The impedance value at the
477 bending point is gradually decreasing. For frequencies above 5 GHz, the maxima shift so far
478 that the impedance curve looks like a horizontal line. In theory, however, such phenomena are
479 not predicted. There is a gradual rise in the wings of the curve after the maxima with increasing
480 frequency, while these maxima remain fixed relative to the field axis. The discrepancy between
481 theory and experiment occurs in the MHz to GHz frequency range which is pivotal for
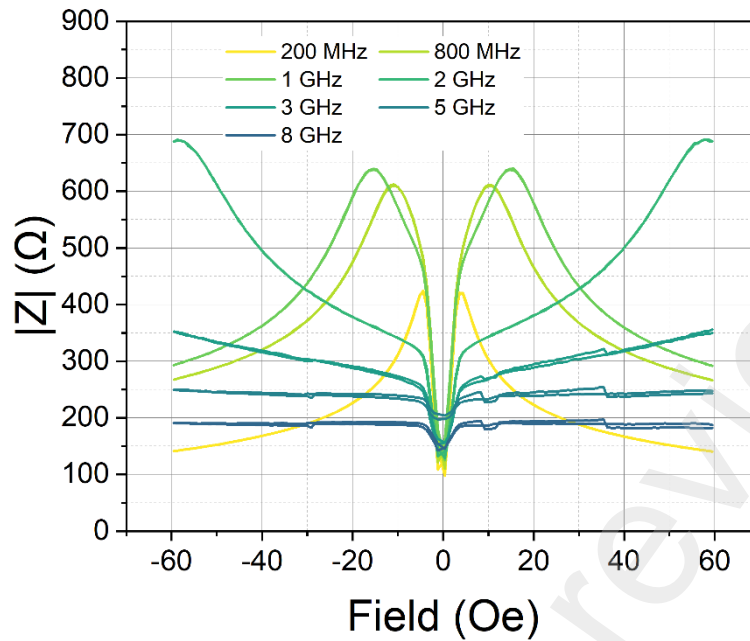482 scattering applications.

The question of how to construct a rigorous scattering theory for wire inclusions remains open. The solution to the internal problem is impossible due to the complex magnetic domain structure. Further progress will be made through the development of hybrid methods in which the external scattering problem is solved numerically along with experimental impedance boundary conditions. The single-particle scattering problem is the first step in this direction. The approach using the antenna integro-differential equation for the wire current does not require the mesh as in more universal finite-element methods [40]. However, the solution of many such equations interlocking through a complex operator of electromagnetic interaction between inclusions would be numerically costly. It would also be worthwhile to explore the extent to which CST can be used for such simulations. In a single-particle problem, we calculated the distribution of the surface circular magnetic field $\overline{H}_\varphi$ along a wire 50 mm long and 19.1 μm in diameter induced by a plane wave (Fig. 14). The 1.5 GHz wave was linearly polarized with an electric field (1 V/m) along the wire. The experimental surface impedance was used as the boundary condition. The field $\overline{H}_\varphi$ is a measure of the total effective current $I = 2\pi a\overline{H}_\varphi$ induced by the wave, which takes zero values at the ends of the wire fulfilling the boundary conditions. A sufficiently dense mesh is required to reduce the simulation error on the surface of the wire. We tried using "the cells per max model box edge" (simulation option in CST) equals 10 or 100. The number 10 provides a non-physical periodical

angular dependence of $\overline{H}_\varphi$ on the wire surface, while it should be constant. The simulations shown in Fig. 14 used 100 cells resulting in a much smaller ripple of $\overline{H}_\varphi$ over the azimuthal angle φ. The field values were obtained by averaging $\overline{H}_\varphi$ over φ for each longitudinal position with a 5 mm step. The simulation has been done on a DELL XPS 8930 computer (i7-9700 CPU@3.00 GHz, RAM 32 GB, Windows 10 Pro, 64-bit operating system). The computation time ranges from seconds to a few minutes depending on the mesh numbers. Using a detailed mesh to model such a thin wire compared to its length and wavelength does not look quite reasonable. This issue should be further addressed.

As the computation power increases, the preferences of researchers will certainly shift toward universal solvers. Therefore, we see broad prospects for using CST for modelling electromagnetic properties of composite structures with wire inclusions. The hybrid approach removes one of the significant obstacles which is finding the solution of the complicated internal problem. The rest is purely an electrodynamic task that dispenses with complex material properties.
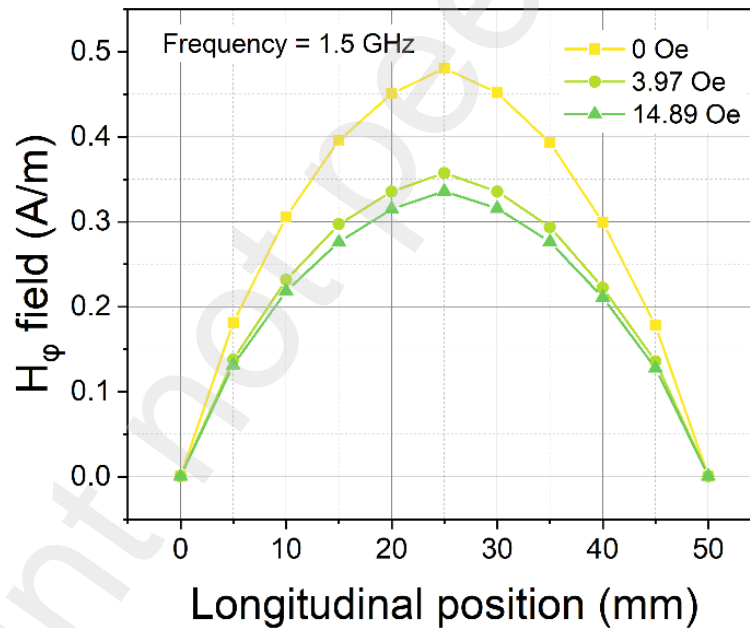

Fig. 14. Distribution of the surface circular magnetic field along a 50 mm wire dipole induced by the plane wave with the electrical field along the wire. The experimental surface impedance was used as the boundary condition at three values of the bias field.

6. Conclusion

We have developed a broadband measurement technique for the surface impedance of ferromagnetic wires up to 15 GHz. It includes a three-stage calibration procedure: SOLT calibration of VNA and coaxial cables, de-embedding of microstrips, and compensation of the delay time (phase incursion) along the wire sample. The impedance is measured on PCB cells to allow external magnetic field, tensile stress, and heating stimuli. De-embedding of microstrips is implemented using the specially designed calibration PCB cells with the surface mount SOL terminations. By measuring three reflection coefficients on the calibration cells and using the 3-term model, the S-parameters of the microstrips can be determined. Compensation of the delay time along the sample was implemented using the phase unwrapping technique. The ability to carry out de-embedding up to 15 GHz made it possible to reduce the uncertainty in determining the delay time to $\pm$ 3 ps. The accuracy of the impedance measurements has been verified by fitting the dispersion model provided by the CST Studio Suite, which ensures meeting the Kramers-Kronig relations. Use of experimental impedance boundary conditions for scattering problems was tested in CST to calculate the current distribution in a wire dipole induced by an electromagnetic wave. The hybrid approach combining experimental material parameters and electrodynamic simulations provide solid ground for designing the microwave response of wire-filled composite materials.

Declaration of Competing Interest

The authors declare that they have no known competing financial interests or personal relationships that could have appeared to influence the work reported in this paper.

References

[1]   L.V. Panina, K. Mohri, Magneto-impedance effect in amorphous wires, Appl. Phys. Lett. 65 (1994) 1189–1191. doi:10.1063/1.112104.

[2]   D. Ménard, M. Britel, P. Ciureanu, A. Yelon, V.P. Paramonov, A.S. Antonov, P. Rudkowski, J.O. Ström-Olsen, High frequency impedance spectra of soft amorphous fibers, J. Appl. Phys. 81 (1997) 4032–4034. doi:10.1063/1.364927.

557   [3]   M. Dominguez, J.M. Garcia-Beneytez, M. Vazquez, S.E. Lofland, S.M. Bhagat,
558   Microwave response of amorphous microwires: Magnetoimpedance and ferromagnetic
559   resonance, J. Magn. Magn. Mater. 249 (2002) 117–121. doi:10.1016/S0304-
560   8853(02)00517-6.

561   [4]   A. Zhukov, L. Gonzalez-Legarreta, M. Ipatov, P. Corte-Leon, J.M. Blanco, V. Zhukova,
562   Giant magnetoimpedance effect at GHz frequencies in amorphous microwires, AIP Adv.
563   9 (2019). doi:10.1063/1.5129891.

564   [5]   J. Alam, M. Nematov, N. Yudanov, S. Podgornaya, L.V. Panina, High-frequency
565   magnetoimpedance (MI) and stress-MI in amorphous microwires with different
566   anisotropies, Nanomaterials. 11 (2021). doi:10.3390/nano11051208.

567   [6]   Z. Zhu, M. Peng, Y. Wang, F.X. Qin, Ultra-large giant magnetoimpedance effect by a
568   2D square spiral amorphous microwire, J. Magn. Magn. Mater. 550 (2022) 169090.
569   doi:10.1016/j.jmmm.2022.169090.

570   [7]   M. Knobel, J. Schoenmaker, J.P. Sinnecker, R.S. Turtelli, R. Grössinger, W. Hofstetter,
571   H. Sassik, Giant magneto-impedance in nanocrystalline $Fe_{73.5}Cu_1Nb_3Si_{13.5}B_9$ and
572         $Fe_{86}Zr_7B_6Cu_1$ ribbons, Mater. Sci. Eng. A. 226–228 (1997) 546–549.
573   doi:10.1016/s0921-5093(96)10682-1.

574   [8]   D. Stanescu, P. Xavier, J. Richard, C. Dubourdieu, Evidence of the magnetoimpedance
575   effect up to microwave frequencies in polycrystalline La0.7Sr0.3MnO3 films, J. Appl.
576   Phys. 99 (2006). doi:10.1063/1.2189202.

577   [9]   K. Agra, T.J.A. Mori, L.S. Dorneles, V.M. Escobar, U.C. Silva, C. Chesman, F. Bohn,
578   M.A. Corrêa, Dynamic magnetic behavior in non-magnetostrictive multilayered films
579   grown on glass and flexible substrates, J. Magn. Magn. Mater. 355 (2014) 136–141.
580   doi:10.1016/j.jmmm.2013.12.009.

581   [10]   A. Chanda, R. Mahendiran, Microwave magnetoimpedance and ferromagnetic
582   resonance in Pr0.6Sr0.4MnO3, RSC Adv. 9 (2019) 29246–29254.
583   doi:10.1039/c9ra06786h.

584   [11]   M. Tejedor, B. Hernando, M.L. Sánchez, V.M. Prida, M. Vázquez, Magneto-impedance
585   effect in amorphous ribbons for stress sensor application, Sensors Actuators, A Phys. 81
586   (2000) 98–101. doi:10.1016/S0924-4247(99)00095-3.

587   [12]   E. Vremera, C. Fosalau, L. Brunetti, Instrumentation set-up for characterisation of the
588   sensors based on amorphous wires, Meas. J. Int. Meas. Confed. 41 (2008) 327–333.
589   doi:10.1016/j.measurement.2006.11.003.

590   [13]   K.N. Choi, Metal detection sensor utilizing magneto-impedance magnetometer, J.

591   Sensors. 2018 (2018). doi:10.1155/2018/3675090.

592   [14]   A. Sayad, E. Skafidas, P. Kwan, Magneto-impedance biosensor sensitivity: Effect and
593   enhancement, Sensors (Switzerland). 20 (2020) 1–20. doi:10.3390/s20185213.

594   [15]   G.Y. Melnikov, V.N. Lepalovskij, A. V. Svalov, A.P. Safronov, G. V. Kurlyandskaya,
595   Magnetoimpedance thin film sensor for detecting of stray fields of magnetic particles in
596   blood vessel, Sensors. 21 (2021) 1–17. doi:10.3390/s21113621.

597   [16]   J.J. Beato-López, J.M. Algueta-Miguel, C. Gómez-Polo, Contactless magnetic
598   nanoparticle detection platform based on non-linear GMI effect, Meas. J. Int. Meas.
599   Confed. 180 (2021). doi:10.1016/j.measurement.2021.109602.

600   [17]   V.S. Larin, A. V Torcunov, A. Zhukov, M. Vazquez, L.V. Panina, Preparation and
601   properties of glass-coated microwires, J. Magn. Magn. Mater. 249 (2002) 39–45.
602   doi:10.1016/S0304-8853(02)00501-2.

603   [18]   O. Reynet, A.L. Adenot, S. Deprot, O. Acher, M. Latrach, Effect of the magnetic
604   properties of the inclusions on the high-frequency dielectric response of diluted
605   composites, Phys. Rev. B - Condens. Matter Mater. Phys. 66 (2002) 944121–944129.
606   doi:10.1103/PhysRevB.66.094412.

607   [19]   D. P. Makhnovskiy, L. V. Panina, Field dependent permittivity of composite materials
608   containing ferromagnetic wires, J. Appl. Phys. 93 (2003) 4120–4129.
609   doi:10.1063/1.1557780.

610   [20]   I. Liberal, I. S. Nefedov, I. Ederra, R. Gonzalo, S. A. Tretyakov, Electromagnetic
611   response and homogenization of grids of ferromagnetic microwires, J. Appl. Phys. 110
612   (2011) 1–8. doi:10.1063/1.3631062.

613   [21]   F.X. Qin, H.X. Peng, Ferromagnetic microwires enabled multifunctional composite
614   materials, Prog. Mater. Sci. 58 (2013) 183–259. doi:10.1016/j.pmatsci.2012.06.001.

615   [22]   L. V. Panina, D.P. Makhnovskiy, Magnetic microwires in microwave applications,
616   Elsevier Ltd., 2015. doi:10.1016/B978-0-08-100164-6.00017-5.

617   [23]   A. Allue, P. Corte-León, K. Gondra, V. Zhukova, M. Ipatov, J.M. Blanco, J. Gonzalez,
618   M. Churyukanova, S. Taskaev, A. Zhukov, Smart composites with embedded magnetic
619   microwire inclusions allowing non-contact stresses and temperature monitoring,
620   Compos. Part A Appl. Sci. Manuf. 120 (2019) 12–20.
621   doi:10.1016/j.compositesa.2019.02.014.

622   [24]   M. Peng, F.X. Qin, Clarification of basic concepts for electromagnetic interference
623   shielding effectiveness, J. Appl. Phys. 225108 (2021) 1–9.
624   https://doi.org/10.1063/5.0075019.

625 [25] H. García-Miquel, M.J. Esbrí, J.M. Andreés, J.M. García, J.M. García-Beneytez, M.
626   Vázquez, Power absorption and ferromagnetic resonance in Co-rich metallic glasses,
627   IEEE Trans. Magn. 37 (2001) 561–564. doi:10.1109/20.914378.

628 [26] A. Vepsalainen, K. Chalapat, G.S. Paraoanu, Measuring the microwave magnetic
629   permeability of small samples using the short-circuit transmission line method, IEEE
630   Trans. Instrum. Meas. 62 (2013) 2503–2510. doi:10.1109/TIM.2013.2259111.

631 [27] S. V. Shcherbinin, S.O. Volchkov, A. V. Svalov, V.O. Vas'kovskii, G. V.
632   Kurlyandskaya, Measurement of the parameters of ferromagnetic microwires in a
633   frequency range from 0.1 to 20 GHz, Inorg. Mater. Appl. Res. 11 (2020) 181–187.
634   doi:10.1134/S2075113320010311.

635 [28] C. Bilzer, T. Devolder, P. Crozat, C. Chappert, S. Cardoso, P.P. Freitas, Vector network
636   analyzer ferromagnetic resonance of thin films on coplanar waveguides: Comparison of
637   different evaluation methods, J. Appl. Phys. 101 (2007) 1–5. doi:10.1063/1.2716995.

638 [29] E. Fernandez, A. Lopez, A. Garcia-Arribas, A. V. Svalov, G. V. Kurlyandskaya, A.
639   Barrainkua, High-frequency magnetoimpedance response of thin-film microstructures
640   using coplanar waveguides, IEEE Trans. Magn. 51 (2015) 4–7.
641   doi:10.1109/TMAG.2014.2359991.

642 [30] M. Kilinc, C. Garcia, M. Eginligil, J. Wang, W. Huang, De-embedding zero-field signal
643   in high-frequency magneto-impedance measurements of soft ferromagnetic materials, J.
644   Magn. Magn. Mater. 484 (2019) 424–429. doi:10.1016/j.jmmm.2019.02.021.

645 [31] J.M. González, A. García-Arribas, S. V. Shcherbinin, V.N. Lepalovskij, J.M. Collantes,
646   G. V. Kurlyandskaya, Broadband ferromagnetic resonance measurements in thin-film
647   structures for magnetoimpedance sensors, Meas. J. Int. Meas. Confed. 126 (2018) 215–
648   222. doi:10.1016/j.measurement.2018.05.070.

649 [32] A.L.R. Souza, M. Gamino, A. Ferreira, A.B. de Oliveira, F. Vaz, F. Bohn, M.A. Correa,
650   Directional field-dependence of magnetoimpedance effect on integrated yig/pt-stripline
651   system, Sensors. 21 (2021) 1–12. doi:10.3390/s21186145.

652 [33] B.C. Wadell, Transmission line design handbook, Artech House Inc, 1991.

653 [34] G. Crupi, D. Schreurs, Microwave de-embedding: From theory to applications,
654   Academic Press, 2013.

655 [35] R. El Kammouni, G. Infante, J. Torrejón, M.R. Britel, J. Brigui, M. Vázquez, Microwave
656   behavior in CoFe-based single- and two-phase magnetic microwires, Phys. Status Solidi
657   Appl. Mater. Sci. 208 (2011) 520–525. doi:10.1002/pssa.201026407.

658 [36] S. V. Shcherbinin, R. Perez, M. Vazquez, G. V. Kurlyandskaya, Ferromagnetic

659   resonance in electroplated CuBe/FeCoNi and amorphous CoFeSiB wires, IEEE Trans.
660   Magn. 56 (2020). doi:10.1109/TMAG.2020.2974141.

661 [37] D. P. Makhnovskiy, L. V. Panina, D. J. Mapps, Field-dependent surface impedance
662   tensor in amorphous wires with two types of magnetic anisotropy: Helical and
663   circumferential, Phys. Rev. B - Condens. Matter Mater. Phys. 63 (2001) 1–17.
664   doi:10.1103/PhysRevB.63.144424.

665 [38] M. Knobel, M. Vázquez, L. Kraus, Giant Magnetoimpedance, K.H.J. Buschow (Ed.),
666   Handb. Magn. Mater., 1st ed., Elsevier Ltd, (2003) 497–563. doi:10.1016/S1567-
667   2719(03)15005-6.

668 [39] Y. Zhao, Y. Wang, D. Estevez, F.X. Qin, H. Wang, X. Zheng, D.P. Makhnovskiy, H.
669   Peng, Novel broadband measurement technique on PCB cells for the field- And stress-
670   dependent impedance in ferromagnetic wires, Meas. Sci. Technol. 31 (2020) 1–8.
671   doi:10.1088/1361-6501/ab4556.

672 [40] A. Uddin, Y. Zhao, F.X. Qin, On hybrid approach in microwave scattering theory for
673   wire-filled composites, 2021 Photonics Electromagn. Res. Symp., IEEE, Hangzhou,
674   (2021) 528–534. doi:10.1109/PIERS53385.2021.9694931.

675 [41] S.D. Jiang, T. Eggers, O. Thiabgoh, D.W. Xing, W.D. Fei, H.X. Shen, J.S. Liu, J.R.
676   Zhang, W.B. Fang, J.F. Sun, H. Srikanth, M.H. Phan, Relating surface roughness and
677   magnetic domain structure to giant magneto-impedance of Co-rich melt-extracted
678   microwires, Sci. Rep. 7 (2017) 1–8. doi:10.1038/srep46253.

679 [42] Rogers Corporation, https://rogerscorp.com/.

680 [43] Joel P. Dunsmore, Handbook of Microwave Component Measurements: with Advanced
681   VNA Techniques, 2012. doi:10.1002/9781118391242.

682 [44] GitHub, https://github.com/DYK-Team/vna-impedance-measurments.

683 [45] L.D. Landau, E.M. Lifshitz, Electrodynamics of Continuous Media, Pergamon Press,
684   1975.

685 [46] S. Sandacci, D.P. Makhnovskiy, L.V. Panina, K. Mohri, Y. Honkura, Off-diagonal
686   impedance in amorphous wires and its application to linear magnetic sensors, IEEE
687   Trans. Magn. 40 (2004) 3505–3511. doi:10.1109/TMAG.2004.835676.

688 [47] D. Estevez, Y. Zhao, Y. Wang, F.X. Qin, H.X. Peng, Optimizing magnetoimpedance of
689   amorphous microwires by nanocarbon-induced magnetic anisotropy, J. Magn. Magn.
690   Mater. 502 (2020) 166527. doi:10.1016/j.jmmm.2020.166527.

691